Ostermeyer, M.; Mudge, D.; Veitch, Peter John; Munch, Jesper.
Thermally induced birefringence in Nd : YAG slab lasers, *Applied Optics*, 2006; 45 (21):5368-5376.

# Thermally induced birefringence in Nd:YAG slab lasers

Martin Ostermeyer, Damien Mudge, Peter J. Veitch, and Jesper Munch

We study thermally induced birefringence in crystalline Nd:YAG zigzag slab lasers and the associated depolarization losses. The optimum crystallographic orientation of the zigzag slab within the Nd:YAG boule and photoelastic effects in crystalline Nd:YAG slabs are briefly discussed. The depolarization is evaluated using the temperature and stress distributions, calculated using a finite element model, for realistically pumped and cooled slabs of finite dimensions. Jones matrices are then used to calculate the depolarization of the zigzag laser mode. We compare the predictions with measurements of depolarization, and suggest useful criteria for the design of the gain media for such lasers. 

*OCIS codes:* 120.6810, 140.3070, 140.3480, 140.3530.

## 1. Introduction

The use of high brightness diode–laser pump sources allow higher gain for a given maximum heat deposition. Together with the reduced cost this has led to new, high power laser developments that avoid lamp pumping, thus avoiding excess heating and notoriously bad beam quality. The high gain that can be achieved with diode–laser pumping has also allowed the development of cw Nd:YAG lasers that use unstable resonators.[1–3] To exploit this capability fully, the increased pumping required ultimately leads back to significant thermal loading and thermally induced birefringence, which depolarizes the laser mode and can cause poor efficiency. Slab gain media are often used to mitigate these effects, as they minimize the impact of thermally induced birefringence and have a higher stress induced fracture limit than rod configurations.[4] They have the additional advantage that they can have Brewster-angled entrance and exit faces, removing the need for antireflection coatings and providing a polarized laser mode. Furthermore, a $\pi(p)$ plane polarized mode can propagate along a zigzag path in the $yz$ plane (see Fig. 1), reducing the strong "thermal lensing" typically encountered with high power loadings.[5] The zigzag path also results in an efficient overlap of the lasing mode with the gain distribution and in beam parameters that are independent of the pump power.

In the ideal slab (see Fig. 1), heat is uniformly generated throughout the slab and the large surfaces (or faces) of the slab are uniformly cooled. The ideal slab is infinitely high ($x$ direction) and long ($z$ direction). Thus there is heat removal in the $y$ direction only, resulting in a 1D temperature gradient. While the birefringence would not depolarize a laser mode propagating along the $z$ axis, it could depolarize a beam propagating along a zigzag path in the $yz$ plane.[4,6] However, this depolarization can be prevented by cutting the slab from the boule with the appropriate crystallographic orientation.[6]

Real slabs are not infinitely high and long, nor are they uniformly pumped or uniformly face cooled. Thermally induced shear stresses thus occur, causing additional birefringence that depolarizes the laser mode.[6] This is particularly relevant for the high gain cw laser heads that are necessary for use with unstable resonators.[1,3,7]

This paper will investigate thermally induced birefringence in practical crystalline Nd:YAG slabs. While only Nd:YAG is considered here, the general principles can be applied to other crystals with a cubic lattice. The stresses are calculated using a finite-element model (FEM) of a Nd:YAG slab that is side pumped and side cooled over only part of the side face so as to maximize gain and enable the use of water seals. The model includes temperature-dependent thermal conductivity and thermal expansion coefficients. We have previously used this model to show that the stresses in such slabs can be a factor of 3 larger than those pre-

M. Ostermeyer (oster@rz.uni-potsdam.de) is with the Institute of Physics, University of Potsdam, 14669 Potsdam, Germany. D. Mudge, P. J. Veitch (peter.veitch@adelaide.edu.au), and J. Munch are with the Department of Physics, The University of Adelaide, Adelaide, South Australia 5005, Australia.

Received 21 December 2005; accepted 22 January 2006; posted 3 February 2006 (Doc. ID 66829).

0003-6935/06/215368-09$15.00/0

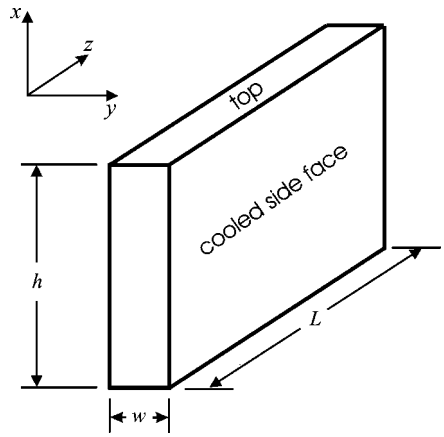


Fig. 1. Ideal slab geometry showing the axes and notation used in this paper. The axes are the same as those used by Eggleston *et al.* (Ref. 4) but different from those used by Lü *et al.* (Ref. 6).

dicted by the usual simplified models.[8] Here we use the results to calculate the depolarization resulting from the thermal stresses within the slab and compare the predictions with measurements.

We shall begin by briefly reviewing the preferred orientation of the zigzag slab within the Nd:YAG boule in Section 2, and the photoelastic effects in crystalline Nd:YAG slabs[6] in Section 3. The thermally induced birefringence is calculated using the dielectric impermeability tensor and the temperature and stress distributions predicted by the FEM. Jones matrices are then used to calculate the depolarization of the laser mode. This procedure is summarized in Section 4, and the numerical predictions are discussed in Section 5. The predictions are compared with measurements in Section 6. The results show that our model provides important insight into the effect of the nonideal pumping and/or cooling profile on thermally induced birefringence and laser mode depolarization.

## 2. Optimum Orientation of Zigzag Slabs Within the Nd:YAG Boule

Nd:YAG crystals are usually grown in a boule using the Czochralski method with a ⟨111⟩ growth axis, as shown in Fig. 2. When the boule is pulled from the melt, a conelike shape results at the top of the boule, and growth rings or striations are produced due to minor fluctuations in the chemical concentration and temperature of the melt. The growth striations are parallel to the surface of the cone in the boule. There is also usually a radial gradient in the dopant concentration.

When a zigzag slab is cut from the boule two conditions should be satisfied: The growth striations should not be parallel to the beam propagation for any segment of the zigzag path and the impact of thermally induced birefringence should be minimized. The slab is usually cut with the long ($z$) axis, parallel to the ⟨111⟩ boule axis. In the case of zigzag slabs (a) and (c) in Fig. 2, the growth striations are almost parallel to the zigzag for some of the path and thus these orientations are unsuitable. The slab location denoted (b) shows a suitable section of the Nd:YAG boule from which zigzag slabs may be harvested. Figure 3 shows

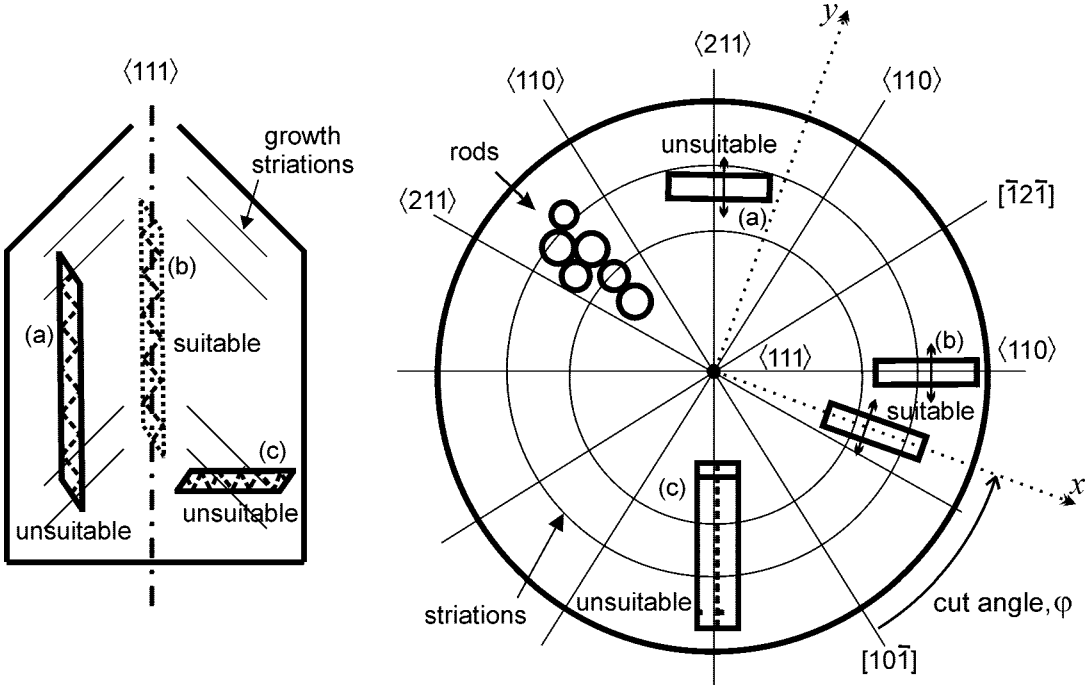


Fig. 2. Suitable and unsuitable orientations for zigzag slabs in a Nd:YAG boule, elevation (left) and top view (right). The slab (b) in the left-hand diagram is located at the perimeter of the boule. The double-arrowed line in slabs (a) and (b) in the right-hand diagram, represent the zigzag direction. The ⟨110⟩ and ⟨211⟩ crystal axes and the equivalent directions are marked. The section of the boule from where cylindrical laser rods are typically harvested is also shown for completeness. The cut angle, φ, is measured relative to the [10$\bar{1}$] direction.

the image of a HeNe laser beam transmitted through zigzag slabs that have suitable and unsuitable crystallographic orientations; the diffraction due to the growth striations is clearly evident. The effect of thermally induced birefringence also varies strongly with orientation within the boule, as will be discussed in the Section 3.

### 3. Photoelastic Effects in Crystalline Nd:YAG

The optical properties of an anisotropic crystal are determined by the dielectric tensor $\varepsilon_{ij}$, where $D_i = \varepsilon_{ij}E_j$ and $\varepsilon_{ij} = \varepsilon_o(1 + \chi_{ij})$ are the well-known relationships from electromagnetic theory.[9,10]

Conservation of energy requires that $\varepsilon_{ij}$ is symmetric. For a transparent, nonmagnetic optical crystal, it is possible to write the surfaces of constant energy density as an ellipsoid in terms of the principal axes of the dielectric tensor,[10]

$$\frac{x^2}{\varepsilon_x} + \frac{y^2}{\varepsilon_y} + \frac{z^2}{\varepsilon_z} = 1.$$

With $n_i^2 = \varepsilon_i/\varepsilon_o$, this is the well-known ellipsoid of wave normals, or "optical indicatrix."

It is convenient to define the relative dielectric impermeability tensor $B_{ij}$ as the inverse of $\varepsilon_{ij}$, resulting in an alternative form of the optical indicatrix[9]:

$$B_x x^2 + B_y y^2 + B_z z^2 = 1,$$

or more generally,

$$B_{ij} x_i x_j = 1.$$

Changes in the refractive index due to temperature and stress can be treated as small changes in $B_{ij}$[6,11]:

$$B_{ij} = B_{o,ij} + \pi_{ijkl}\,\sigma_{kl}, \tag{1}$$

where

$$B_{o,ij} = \delta_{ij} \Big/ \left\{ n_o + \frac{\mathrm{d}n}{\mathrm{d}T}\,[T(x, y, z) - T_o] \right\}^2,$$

$\pi_{ijkl}$ is the piezo-optic tensor, and $\sigma_{kl}$ is the stress tensor. Thus an applied stress will change $B_{ij}$ and rotate the indicatrix, leading to a change in the birefringence of the crystal.

For a Nd:YAG slab in which the $z$ axis is in the [111] direction, the $x$ axis is at an angle of $\varphi$ to the $[10\bar{1}]$ direction, and the $y$ axis is at an angle of $\varphi$ to the $[\bar{1}2\bar{1}]$ direction (see Fig. 2). Equation (1) can be written[6]

$$\begin{bmatrix} B_{11} \\ B_{22} \\ B_{33} \\ B_{23} \\ B_{13} \\ B_{12} \end{bmatrix} = \begin{bmatrix} B_{0,11} \\ B_{0,22} \\ B_{0,33} \\ 0 \\ 0 \\ 0 \end{bmatrix} + \begin{bmatrix} \pi_{11} & \pi_{12} & \pi_{13} & \pi_{14} & \pi_{15} & 0 \\ \pi_{12} & \pi_{11} & \pi_{13} & -\pi_{14} & -\pi_{15} & 0 \\ \pi_{13} & \pi_{13} & \pi_{33} & 0 & 0 & 0 \\ \pi_{14} & -\pi_{14} & 0 & \pi_{44} & 0 & -\pi_{15} \\ \pi_{15} & -\pi_{15} & 0 & 0 & \pi_{44} & \pi_{14} \\ 0 & 0 & 0 & -\pi_{15} & \pi_{14} & \pi_{66} \end{bmatrix} \begin{bmatrix} \sigma_{11} \\ \sigma_{22} \\ \sigma_{33} \\ \sigma_{23} \\ \sigma_{13} \\ \sigma_{12} \end{bmatrix}, \tag{2}$$

where the values of $\pi_{ij}$ for Nd:YAG (measured at 632.8 nm) are[6,12]

$$\begin{aligned}
\pi_{11} &= -0.30285 \times 10^{-12}\ \mathrm{m^2\ N^{-1}},\\
\pi_{12} &= +0.11158 \times 10^{-12}\ \mathrm{m^2\ N^{-1}},\\
\pi_{13} &= +0.17187 \times 10^{-12}\ \mathrm{m^2\ N^{-1}},\\
\pi_{33} &= -0.36313 \times 10^{-12}\ \mathrm{m^2\ N^{-1}},\\
\pi_{44} &= -0.14693 \times 10^{-12}\ \mathrm{m^2\ N^{-1}},\\
\pi_{66} &= -0.20722 \times 10^{-12}\ \mathrm{m^2\ N^{-1}},\\
\pi_{14} &= -0.08525 \times 10^{-12} \cos(3\varphi)\ \mathrm{m^2\ N^{-1}},\\
\pi_{15} &= -0.08525 \times 10^{-12} \sin(3\varphi)\ \mathrm{m^2\ N^{-1}},
\end{aligned}$$

Thus for a zigzag slab in which the mode is incident upon the cooled surfaces with an angle $\theta$ as shown in Fig. 4(a), the relative dielectric impermeability tensor can be determined by rotating $B$ (to $B'$) by an angle $\gamma = \pi/2 - \theta$ around the $x$ axis,[6] giving

$$B_{11}' = B_{11},$$

$$B_{22}' = B_{22}\cos^2\gamma + 2B_{23}\cos\gamma\sin\gamma + B_{33}\sin^2\gamma,$$

$$B_{12}' = B_{21}' = B_{12}\cos\gamma + B_{13}\sin\gamma.$$

Substituting from Eq. (2) gives

$$\begin{aligned}
B_{12}' &= \cos\gamma[-\sigma_{23}\pi_{15} + \sigma_{13}\pi_{14} + \sigma_{12}\pi_{66}]\\
&\quad + \sin\gamma[(\sigma_{11} - \sigma_{22})\pi_{15} + \sigma_{13}\pi_{44} + \sigma_{12}\pi_{14}]\\
&= \cos\gamma[-\sigma_{yz}\pi_{15} + \sigma_{xz}\pi_{14} + \sigma_{xy}\pi_{66}]\\
&\quad + \sin\gamma[(\sigma_{xx} - \sigma_{yy})\pi_{15} + \sigma_{xz}\pi_{44} + \sigma_{xy}\pi_{14}].
\end{aligned} \tag{3}$$

For an ideal zigzag slab, $B_{12}' = \sin\gamma[(\sigma_{11} - \sigma_{22})\pi_{15}] \propto \sin(3\varphi)$, and thus depolarization can be prevented by using a cut angle, $\varphi$, that is a multiple of 60°. That is, the $y$ axis of the slab could be in, for example, the $[\bar{1}2\bar{1}]$ direction.

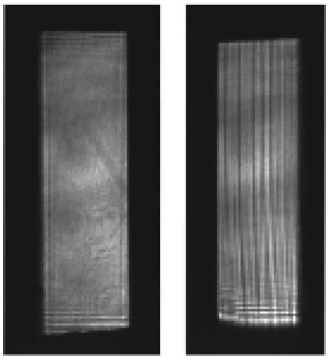

Fig. 3. Imaged transmission at the exit face of a zigzag slab with suitable (left) and unsuitable (right) orientations. The growth striations in the right image are visible as some parts of the zigzag path is almost parallel to the growth striations.

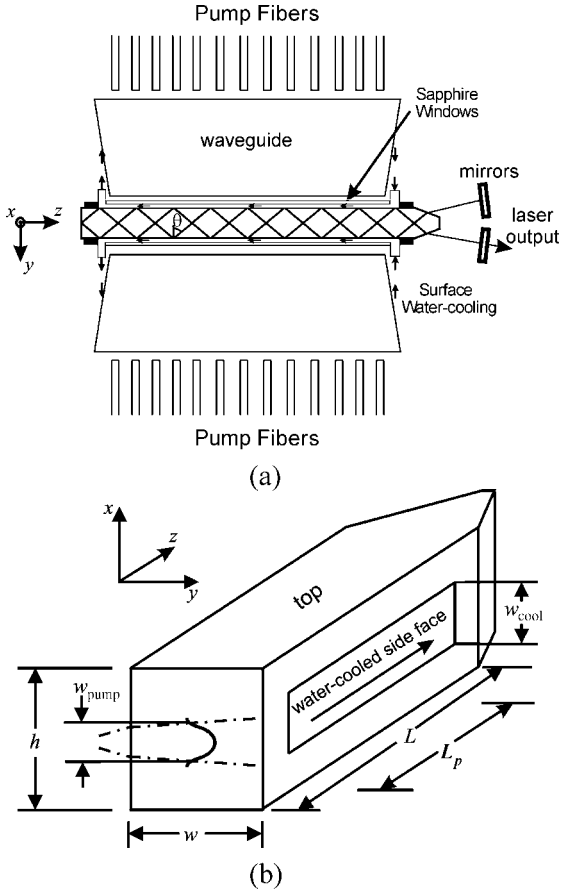


Fig. 4. (a) Pump architecture and beam path through a side-pumped, side-cooled CPFS laser. The waveguides smooth the intensity profile of the pump distribution in the plane of the page but preserve the numerical aperture of the pump light in the perpendicular ($x$) direction. (b) Geometrical parameters used in the FEM of the side-pumped, side cooled CPFS. The slab is pumped and cooled on both sides. $w_{\mathrm{pump}}$ is the full height of the pump profile in the slab. $L_p$ is the length of the pumped region. The cooling water flows along a channel that is $w_{\mathrm{cool}}$ high and $L_p$ long. All other slab surfaces are assumed to be insulated.

#### 4. Mode Depolarization in a Realistic Zigzag Slab

The temperature and stress distributions in our real zigzag slab are determined using a FEM that incorporates realistic pump light absorption, realistic cooling, and temperature-dependent thermal conductivity and thermal expansion coefficients. The slab width is chosen to ensure efficient absorption of the pump light, low thermal resistance, and good mechanical stability. In this paper we consider a 1.1 at. % doped Nd:YAG coplanar folded zigzag slab[13] (CPFS) that is side pumped and side cooled. Figure 4(a) shows a top view of the pump architecture and the beam path through a CPFS. Figure 4(b) defines the geometrical parameters used in the model. The slab is coated with Teflon AF (Ref. 14) to prevent disruption of the total internal reflection (TIR) of the zigzag mode due to water seals at the side faces. The temperature in the slab is greater than the cooling water temperature (298 K) because of poor thermal conductivity of the Teflon coating and the limited heat removal efficiency of the flowing water. This will be discussed further in Section 5. The design of this laser head and comparison of the predictions of the FEM with analytical results have been reported in detail elsewhere.[8,15]

We have constructed a 2D and a 3D FEM. The 2D model can be used to calculate the temperature and stress distributions at high resolution for a cross section perpendicular to the $z$ axis. End effects cannot be modeled with the 2D model, and we thus use the lower resolution 3D model to investigate the effect of the finite length of the slab.

The calculated stress distribution is used to determine the components of the relative dielectric impermeability tensor for the zigzag path. The change in the $B_{ij}$ components due to the temperature dependence is neglected as it is small and will have negligible effect on the eigenvalues and eigenvectors of the $B$ submatrix. Jones matrices are used to calculate the change in polarization of a mode. In zigzag and CPFS slabs, this mode is usually $\pi$ polarized. As discussed in Section 3, for an ideal slab there will be a 1D temperature gradient in the $y$ direction. As a consequence, the $y$-stress components are zero and the stresses in the $x$ and $z$ directions are equal.[16] Thus we consider only the depolarization as a function of height ($x$ direction). We also assume that the probe beam is collimated in this analysis.

In detail, the calculation includes the following steps:

(i) The beam propagation between adjacent total internal reflections is divided into 20 propagation steps of length $\Delta$. At each step, the relative dielectric impermeability tensor, $B'$, is calculated from the stress distribution at 101 locations along the vertical ($x$) direction.

(ii) At each location, the eigenvalues, $\lambda_{\pm}$, and (unnormalized) eigenvectors, $\bar{u}_{\pm}$, of the submatrix of $B'$ that is transverse to the beam propagation direction,

$$\begin{bmatrix} B_{11}' & B_{12}' \\ B_{12}' & B_{22}' \end{bmatrix},$$

are calculated using

$$\lambda_{\pm} = \frac{1}{2}\left[(B_{11}' + B_{22}') \pm \sqrt{(B_{11}' - B_{22}')^2 + 4B_{11}'^2}\right], \quad \text{and}$$

$$\mathbf{u}_{\pm} = \begin{bmatrix} 1 \\ \left(\frac{\lambda_{\pm} - B_{11}'}{B_{12}'}\right) \end{bmatrix}.$$

The refractive indices corresponding to these eigenvalues are given by $n_{\pm} = 1/\sqrt{\lambda_{\pm}}$.

(iii) The Jones matrices in the coordinate system defined by the eigenvectors are calculated at each location within the step using

$$J = \begin{bmatrix} \exp(-ikn_{-}\Delta) & 0 \\ 0 & \exp(-ikn_{+}\Delta) \end{bmatrix},$$

where $k$ is the wavenumber.

(iv) These Jones matrices are transformed into the zigzag (primed) coordinate system using

$$J' = R(-\beta)JR(\beta),$$

where

$$R(\beta) = \begin{bmatrix} \cos\beta & \sin\beta \\ -\sin\beta & \cos\beta \end{bmatrix}$$

and $\beta$, the angle between the $x$ axis and the $\mathbf{u}_{-}$ direction, is calculated using

$$\cos\beta = \frac{\mathbf{u}_{-} \cdot \begin{bmatrix} 1 \\ 0 \end{bmatrix}}{|\mathbf{u}_{-}|} = 1 \Big/ \left[1 + \left(\frac{\lambda_{-} - B_{11}'}{B_{12}'}\right)^2\right]^{1/2}$$

[$\beta > 0$ corresponds to the $(u_{-}, u_{+})$ coordinate system being rotated anticlockwise relative to the $(x', y')$ coordinate system].

(v) We assume that the Jones matrix for the TIR, $J_{\mathrm{TIR}}$, is given by

$$J_{\mathrm{TIR}} = \begin{bmatrix} \dfrac{\sin(\gamma) - i\sqrt{\cos(\gamma)^2 - n_r^2}}{\sin(\gamma) + i\sqrt{\cos(\gamma)^2 - n_r^2}} & 0 \\ 0 & \dfrac{n_r^2\sin(\gamma) - i\sqrt{\cos(\gamma)^2 - n_r^2}}{n_r^2\sin(\gamma) + i\sqrt{\cos(\gamma)^2 - n_r^2}} \end{bmatrix},$$

where $n_r$ is the isotropic refractive index of Nd:YAG.

(vi) The total Jones matrix, $J_{\mathrm{total}}$, for the propagation though the gain medium is calculated using

$$J_{\mathrm{total}} = \left[\prod_{m=p}^{1}\left(J_{20}{}^{m\prime}J_{19}{}^{m\prime}, \ldots, J_{1}{}^{m\prime}J_{\mathrm{TIR}}\right)\right] \times \left(J_{20}{}^{m\prime}, \ldots, J_{11}{}^{m\prime}J_{\mathrm{TIR}}J_{10}{}^{m\prime}, \ldots, J_{1}{}^{m\prime}\right) \times \left[\prod_{m=1}^{p}\left(J_{\mathrm{TIR}}J_{20}{}^{m\prime}J_{19}{}^{m\prime}, \ldots, J_{1}{}^{m\prime}\right)\right],$$

where $p$ is the number of total internal reflections on each side face [eg, $p = 9$ in Fig. 4(a).] The total Jones matrix consists of three parts: From the Brewster-angled input face to the TIR just before the blunt end of the slab, the TIR at the blunt end, and from the TIR just after the blunt end to the output Brewster face.

(vii) The transmitted electric field is calculated using $\mathbf{E}_{\mathrm{out}} = J_{\mathrm{total}}\mathbf{E}_{\mathrm{in}}$ and the depolarization loss evaluated.

## 5. Numerical Results

As discussed in Section 3, there will be no depolarization of a $\pi$-polarized mode in an ideal zigzag slab that has a suitable crystallographic orientation. However, the finite height and nonuniform pumping of a practical zigzag slab result in shear stresses that cause depolarization. In this section, we discuss the impact of the finite slab height (or aspect ratio), cut angle, and the nonuniform pumping and cooling of a zigzag slab. This is done by incorporating the stresses predicted by a 2D FEM[17] into the birefringence calculation described in Section 4. We define the transmission as the fraction of a $\pi$-polarized input beam transmitted through a $\pi$-oriented polarizer (analyzer) placed after the slab. The $\pi$-polarized probe laser beam is assumed to have a top-hat profile and a diameter equal to that of the pump beam.

### A. Depolarization Due to Finite Slab Height

The predicted maximum temperature, $T_{\max}$, stresses $\sigma_{xx,\max}$, $\sigma_{yy,\max}$, and shear stress $\sigma_{xy,\max}$ for infinitely long, optimum cut angle, uniformly pumped, and face-cooled slabs with heights of $h = 4.3$ mm and $h = 43$ mm are listed in Table 1. Contour plots of the temperature, $\sigma_{xx}$ and $\sigma_{xy}$ for the $h = 4.3$ mm slab are shown in Fig. 5.

Table 1. Maximum Temperature and Stresses for Two Infinitely Long, Optimum Cut Angle, Uniformly Pumped and Face-Cooled Slabs[a]

| Slab height ($h$) | $T_{max}$ [K] | $\sigma_{xx}$,max [Mpa] | $\sigma_{yy}$,max [Mpa] | $\sigma_{xy}$,max [Mpa] |
|---|---|---|---|---|
| 43 mm | 431 | 130 | 16.4 | 13.3 |
| 4.3 mm | 431 | 146 | 108 | 28 |

[a]The slabs have heights of 4.3 and 43 mm. The width is $w$ = 3 mm and the pump density is 672 MW/m$^3$. $\sigma_{xz} = 0$ and $\sigma_{yz} = 0$ as expected.

The edge temperature of 354 K is higher than the coolant due to the poor thermal conductivity of the cooling interface as discussed earlier. While it is interesting to note the large reduction in $\sigma_{yy,max}$ owing to the increase in slab aspect ratio, we are more concerned with the maximum value of the shear stress $\sigma_{xy,max}$, which decreases only by a factor of approximately 2. However, the nonzero shear stresses in the large aspect-ratio example are concentrated near the top and bottom edges of the slab, as discussed further in the following sections. The shear stresses occupy a smaller fraction of the slab cross section and are further from the center, compared to those for the small aspect-ratio slab. That is, the depolarization losses due to shear stresses can be reduced by increasing the slab aspect ratio.

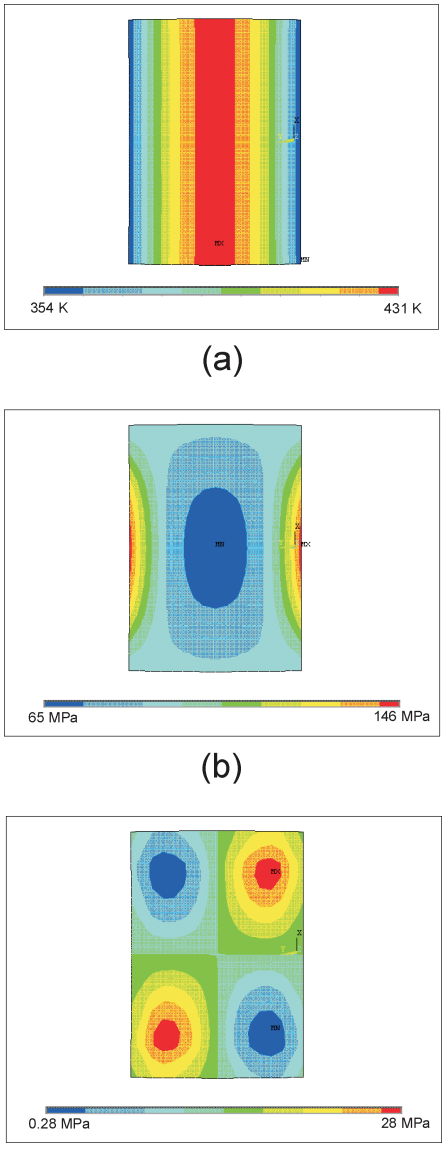


Fig. 5. (Color online) (a) temperature, (b) $\sigma_{xx}$, and (c) $\sigma_{xy}$ for the $h$ = 4.3 mm high slab.

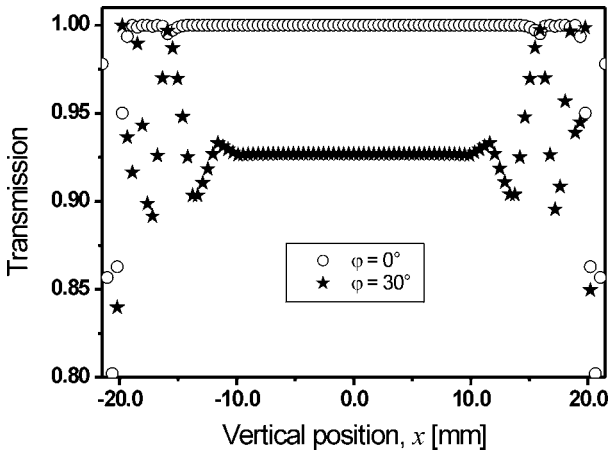


Fig. 6. Predicted transmission through parallel polarizers for an infinitely long, uniformly pumped, and cooled slab, $h$ = 43 mm and $w$ = 3.0 mm. Cut angles $\varphi$ = 0° and 30°.

## B. Depolarization Due to Nonoptimum Cut Angle

The effect of the cut angle on the transmitted intensity for infinitely long, uniformly pumped, and face-cooled slabs with heights of $h$ = 43 mm and $h$ = 4.3 mm is plotted in Figs. 6 and 7, respectively. The same pump density was used for both slabs. Note in Fig. 6 the concentration of the depolarization near the top and bottom edges of the slab, which is in agreement with the previous discussion, and the low depolarization near the center for the 0° cut angle.

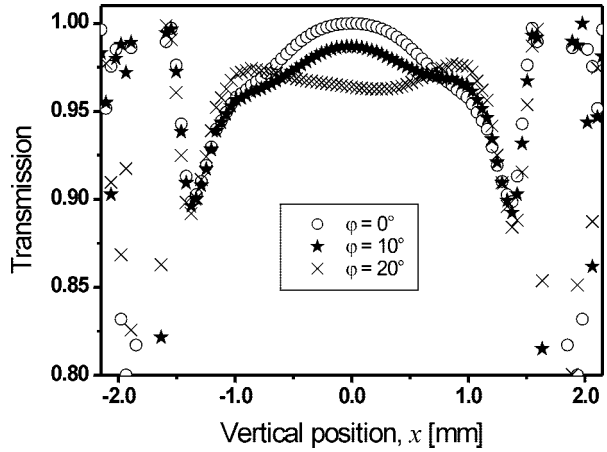


Fig. 7. Predicted transmission through parallel polarizers for an infinitely long, uniformly pumped, and cooled slab, $h$ = 4.3 mm and $w$ = 3 mm. Cut angles $\varphi$ = 0°, 10°, and 20°.

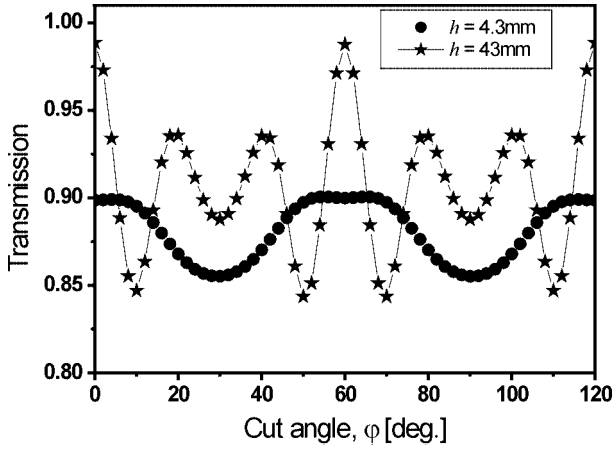


Fig. 8. Integrated transmission through parallel polarizers as a function of the cut angle, for the $h = 43$ mm and $h = 4.3$ mm slabs.

There is no extended low depolarization region within the small aspect-ratio slab, even for $\varphi = 0°$, and the depolarization increases as $\varphi$ approaches 30°. For $\varphi = 60°$ (not shown in Figs. 6 and 7), the result of $\varphi = 0°$ is reproduced, as expected.

The dependence of the integrated depolarization loss on cut angle for the small ($h = 4.3$ mm) and large ($h = 43$ mm) aspect-ratio slabs is plotted in Fig. 8. In both instances a cut angle of 0° or 60° is best. For the $h = 4.3$ mm slab, the transmission is limited to ~90% due to the depolarization resulting from the high $xy$ shear stress. For the $h = 43$ mm slab, the $3\varphi$ dependence can be observed, and almost 100% transmission is achieved at multiples of 60°.

### C. Depolarization Due to Nonuniform Pumping and Cooling

Until now, the examples used have assumed uniform pumping and face cooling. However, in practice, the side pumping is not uniform, and in our case more appropriately represented by a Gaussian profile. Furthermore, if water cooled, the slab requires the use of a gasket or O-ring, and thus the entire slab face is not uniformly cooled. This section considers the impact on shear stress and birefringence resulting from this type of pumping and cooling, assuming that $\varphi = 0°$.

**Table 2. Maximum Stress Levels for Slabs with Different Pump and Cooling Heights, for slab $h = 4.3$ mm and $w = 3.0$ mm[a]**

| Slab | Pump profile | $w_{cool}$ [mm] | $w_{pump}$ [mm] | $\sigma_{xx}$,max [MPa] | $\sigma_{xy}$,max [MPa] | $T$ [%] |
|---|---|---|---|---|---|---|
| gw11 | Gaussian | 1.4 | 1.4 | 144 | 22.6 | 98.5 |
| gw22 | Gaussian | 2 | 2 | 128 | 20.7 | 98.5 |
| gw33 | Gaussian | 3 | 3 | 109 | 17.7 | 91.5 |

[a]The model assumes an incident pump power of 500 W, with 354 W being absorbed in the single pass resulting in 85 W of heating (due to the quantum defect of Nd:YAG). $w_{cool}$ denotes the height of the water channel, and $w_{pump}$ is the diameter of the Gaussian pump profile in the vertical ($x$) direction [see Fig. 4(b)]. $T$ denotes the integrated transmission of a top-hat beam with diameter $w_{pump}$ passing through the zigzag slab located between parallel polarizers.

The transmission profiles for the three different pump and cooling heights are shown in Fig. 9. These examples use Gaussian pump profiles of heights 1.4, 2, and 3 mm, and are labeled gw11, gw22, and gw33, respectively. The width of the central, low depolarization zone in Fig. 9 broadens as the pump and cooling channel becomes larger. However, the broadening is small compared to the increase in the pump and cooling dimension. Predicted values of shear stress within the slab and the transmission of a top-hat probe beam are shown in Table 2. The width of the probe beam used is the same as the full width of the Gaussian pump beam, $w_{pump}$. Although the $xy$ shear stress decreases as $w_{pump}$ increases, the transmission also decreases. This is due to the probe beam traveling through regions of depolarization near the edges of the pump region where the shear stresses build up. Thus to minimize the depolarization loss, pump and probe beams that are less than 50% of the height of the slab should be used, providing that the slab does not fracture.

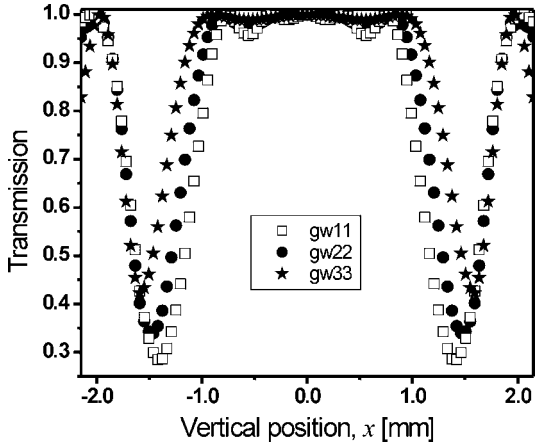


Fig. 9. Predicted transmission through parallel polarizers for different pump and cooling heights and a Gaussian pump profile. The parameters for gw11, gw22, and gw33 are given in Table 2. Slab $h = 4.3$ mm and $w = 3$ mm.

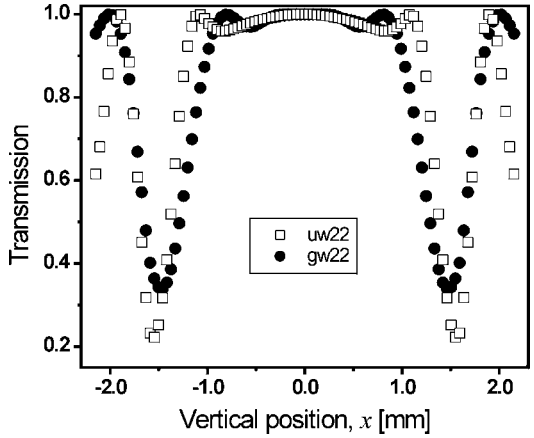


Fig. 10. Predicted transmission through parallel polarizers resulting from a top-hat pump profile (uw22) and a Gaussian pump profile (gw22), for slab $h = 4.3$ mm. The parameters for uw22 and gw22 are given in Table 3.

Table 3. Maximum Stresses for Slabs ($h$ = 4.3 mm and $h$ = 8.6 mm) with Different Pump and Cooling Geometries Using Top-Hat (uw) and Gaussian (gw) Pump Profiles[a]

| Slab | Pump profile | $h$ [mm] | $w_{cool}$ [mm] | $w_{pump}$ [mm] | $\sigma_{xx}$,max [MPa] | $\sigma_{xy}$,max [MPa] | $T$ [%] |
|---|---|---|---|---|---|---|---|
| uw22 | Top hat | 4.3 | 2 | 2 | 122 | 20.2 | 98 |
| gw22 | Gaussian | 4.3 | 2 | 2 | 128 | 20.7 | 98.5 |
| uw66 | Top hat | 8.6 | 6.0 | 6.0 | 144 | 22.6 | 99 |
| gw66 | Gaussian | 8.6 | 6.0 | 6.0 | 109 | 17.7 | 90 |

[a]The model assumes an incident pump power of 500 W, with 354 W being absorbed in the single pass resulting in 85 W of heating (due to the quantum defect of Nd:YAG). $h$ the height of the crystal, $w_{cool}$ denotes the height of the water channel, and $w_{pump}$ is the diameter of the pump profile in the vertical ($x$) direction [see Fig. 4(b)]. $T$ denotes the integrated transmission of a polarized top-hat beam with diameter $w_{pump}$ passing through the zigzag slab located between parallel polarizers.

Changing the pump profile to a top hat moves the shear stresses further from the center of the slab, as shown in Fig. 10, but does not significantly change the depolarization loss for the small aspect-ratio slab. The slab with the top-hat pump profile is labeled uw22. The improvement is more significant in higher aspect-ratio slabs with higher pump regions, as shown in Table 3 and Fig. 11. This large reduction in depolarization loss for the top-hat pump will enable the lasing mode to extract energy more efficiently from the edges of the pumped volume, thus improving lasing efficiency.

### 6. Comparison with Measurements

A zigzag CPFS slab, shown in Fig. 4, with parameters given in Table 4, was used for the measurements. It was pumped using fiber-coupled diode lasers, and planar waveguides were used to smooth the intensity profile of the pump distribution in the $z$ direction. The design of this laser has been reported in detail elsewhere.[8,15] The pump light emerging from the waveguide was measured and is well described by a Gaussian profile with a divergence equal to the 0.22 numerical aperture of the pump fibers.

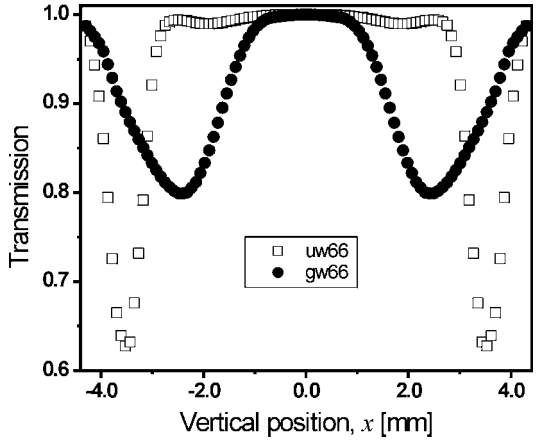


Fig. 11. Predicted transmission through parallel polarizers resulting from a top-hat pump profile (uw66) and a Gaussian pump profile (gw66), for slab $h$ = 8.6 mm. The parameters for uw66 and gw66 are given in Table 3.

Table 4. Dimensions of the Side-Pumped, Side-Cooled Zigzag CPFS Slab Used in the Experiment

| Pump profile | $L$ [mm] | $L_p$ [mm] | $h$ [mm] | $w$ [mm] | $w_{cool}$ [mm] | $w_{pump}$ [mm] | Cut angle $\varphi$ |
|---|---|---|---|---|---|---|---|
| Gaussian | 32.9 | 22 | 4.3 | 3.0 | 2.0 | 2.0 | 0° |

The experiment configuration used to measure the depolarization is shown in Fig. 12. To distinguish between the gain and depolarization loss we measure the depolarization using a 632.8 nm HeNe probe beam that filled the slab. While the HeNe wavelength will not experience identical depolarization to the lasing wavelength (owing to a small shift in refractive index and possible weak wavelength dependence of the $\pi_{ij}$ terms[9]), it is a useful and convenient method to detect the presence and spatial distribution of depolarization and thus provide qualitative validation of the FEM. The slab is located between crossed polarizers, P1 and P2, and the transmitted probe beam was imaged onto the CCD. The depolarization was measured while the gain medium was lasing to ensure that the heat deposition was dominated by pump absorption and to relate the measurements to observed lasing efficiency.

The measured vertical ($x$) transmission through crossed polarizers is compared to the predictions in Fig. 13, showing good qualitative agreement. Regions of high transmission indicate strong depolarization of the probe beam. Both show a double lobe structure with significant birefringence at the edge of the pumped region producing ~50% transmission through crossed polarizers. The asymmetry between the measured transmission at $x = -1.0$ mm and $x = 1.0$ mm is due to asymmetric thermal lensing within the slab, resulting from nonideal boundary conditions. The measurements also indicate the emergence of two smaller lobes of birefringence near the top and bottom edges of the slab, as is predicted by the FEM. The two small lobes measured near $x = 0$ emerge at lower pump powers than predicted by the FEM. The distortion in the horizontal scale of the measurements is probably

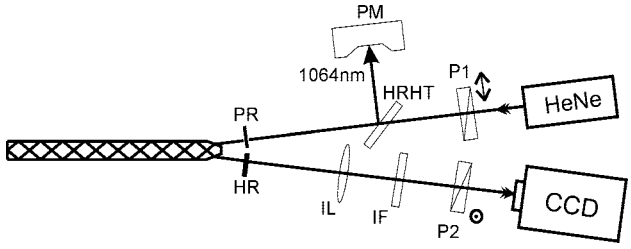


Fig. 12. Experiment used to measure the depolarization of a HeNe probe beam. P1 and P2, input and output crossed polarizers; IF, interference filter; PM, power meter; IL, imaging lens; HR, high reflectivity laser mirror at 1064 nm; CCD, charge coupled-device camera; PR, partially reflective laser mirror at 1064 nm; HRHT, dichroic beam splitter having high reflectivity at 1064 nm and high transmission at 632.8 nm.

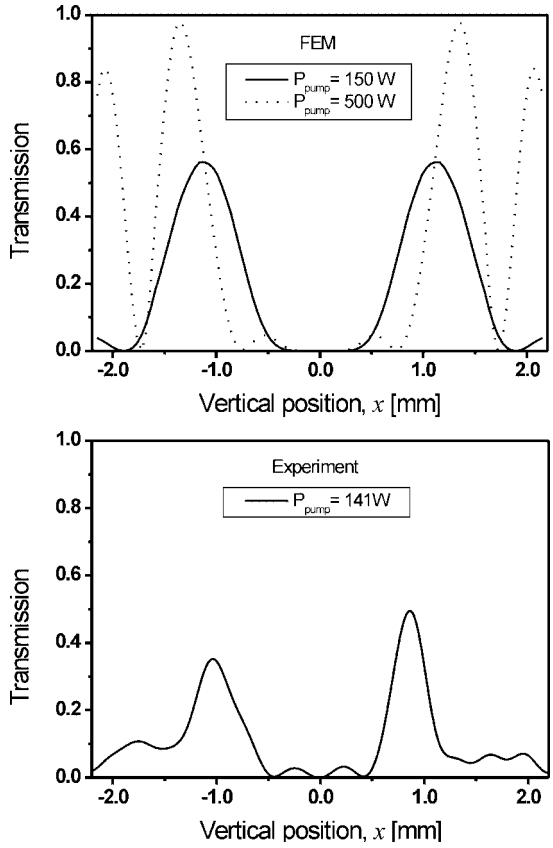


Fig. 13. Predicted (upper) and measured (lower) transmission profiles through crossed polarizers for the Nd:YAG slab shown in Fig. 4. The measured depolarization used the setup shown in Fig. 12. High transmission indicates strong depolarization.

due to focusing of the probe beam by the thermal lens, which was significant at pump powers greater than several tens of watts. This lensing was not included in the model.

## 7. Conclusion

Thermally induced birefringence can significantly reduce the efficiency of high power zigzag slab lasers. The FEM described in this paper provides useful criteria for the design of the gain medium for such lasers. The loss due to depolarization is minimized by using slabs that have the correct crystallographic orientation and have large aspect ratios. Further improvement is gained using top-hat pump profiles and laser modes that do not extend to the top and bottom edges of the slab. Using a top-hat pump profile rather than a Gaussian pump profile significantly reduces the depolarization encountered by the laser mode and increases the volume of the slab in which the depolarization is low. If a Gaussian pump profile is used then it is essential that the pump and laser mode are concentrated near the center of the gain medium, away from the regions where the shear stresses are concentrated.

This research was supported by the Australian Research Council. M. Ostermeyer was supported by the Alexander von Humboldt Foundation. We gratefully acknowledge useful discussions concerning the propagation algorithms with Alexander Hemming of The University of Adelaide.

## References and Notes

1. D. Mudge, P. J. Veitch, J. Munch, D. Ottaway, and M. W. Hamilton, "High-power diode-laser-pumped cw solid-state lasers using stable–unstable resonators," IEEE J. Sel. Top. Quantum Electron. **3,** 19–26 (1997).
2. K. Du, N. Wu, J. Xu, J. Giesekus, P. Loosen, and R. Poprawe, "Partially end-pumped Nd:YAG slab laser with a hybrid resonator," Opt. Lett. **23,** 370–372 (1998).
3. H. Baker, A. A. Chesworth, D. Pelaez Millas, and D. R. Hall, "A planar waveguide Nd:YAG laser with a hybrid waveguide-unstable resonator," Opt. Comm. **191,** 125–131 (2001).
4. J. M. Eggleston, T. J. Kane, K. Kuhn, J. Unternahrer, and R. L. Byer, "The slab geometry laser—Part I: theory," IEEE J. Quantum Electron. **QE-20,** 289–301 (1984).
5. T. J. Kane, R. C. Eckardt, and R. L. Byer, "Reduced thermal focusing and birefringence in zigzag slab geometry crystalline lasers," IEEE J. Quantum Electron. **QE-19,** 1351– 1354 (1983).
6. Q. Lü, U. Wittrock, and S. Dong, "Photoelastic effect in Nd:YAG rod and slab lasers," Opt. Laser Technol. **27,** 95–101 (1995).
7. A. Faulstich, H. J. Baker, and D. R. Hall, "Face pumping of thin, solid-state slab lasers with laser diodes," Opt. Lett. **21,** 594–596 (1996).
8. D. Mudge, M. Ostermeyer, P. J. Veitch, J. Munch, B. Middlemiss, D. J. Ottaway, and M. W. Hamilton, "Power scalable $TEM_{oo}$ cw Nd:YAG laser with thermal lens compensation," IEEE J. Sel. Top. Quantum Electron. **6,** 643–649 (2000).
9. J. F. Nye, *Physical Properties of Crystals* (Oxford Science Publications, 2000).
10. M. Born and E. Wolf, *Principles of Optics* (Pergamon Press, 1970).
11. W. Koechner and D. K. Rice, "Effect of birefringence on the performance of linearly polarized YAG:Nd lasers," IEEE J. Quantum Electron. **QE-6,** 557–566 (1970).
12. R. W. Dixon, "Photoelastic properties of selected materials and their relevance for applications to acoustic light modulators and scanners," J. Appl. Phys. **38,** 5149–5153 (1967).
13. J. Richards and A. McInnes, "Versatile, efficient, diode-pumped miniature slab laser," Opt. Lett. **20,** 371–373 (1995).
14. Teflon AF (1601) is an amorphous fluoropolymer solution developed by DuPont Fluoroproducts, P.O. Box 80711, Wilmington, Dela. 19880–0711.
15. D. Mudge, M. Ostermeyer, D. J. Ottaway, P. J. Veitch, J. Munch, and M. W. Hamilton, "High-power Nd:YAG lasers using stable–unstable resonators," Class. Quantum Grav. **19,** 1783–1792 (2002).
16. D. C. Brown, "Nonlinear thermal and stress effects and scaling behavior of YAG slab amplifiers," IEEE J. Quantum Electron. **34,** 2393–2402 (1998).
17. ANSYS finite-element software, Vers. 5.5.3, http://www.ansys.com/.